1 Variation of sediment supply by periglacial debris flows at Zelunglung
2 in the eastern syntaxis of Himalayas since the 1950 Assam Earthquake

3 Kaiheng Hu[1, 2], Hao Li[1, 2, 3], Shuang Liu[1, 2], Li Wei[1, 2], Xiaopeng Zhang[1, 2, 3], Limin Zhang[4], Bo Zhang[1, 2],
4 Manish Raj Gouli[1, 2, 3]

5 [1]Key Laboratory of Mountain Hazards and Earth Surface Processes, Chinese Academy of Sciences, Chengdu, 610041, China
6 [2]Institute of Mountain Hazards and Environment, Chinese Academy of Sciences, Chengdu, 610041, China
7 [3]University of Chinese Academy of Sciences, Beijing 100049, China
8 [4]Department of Civil and Environmental Engineering, The Hong Kong University of Science and Technology, Clear Water
9 Bay, Hong Kong, China

10 *Correspondence:* Kaiheng Hu (khhu@imde.ac.cn)

11 **ABSTRACT.** Periglacial debris flows boosted by strong earthquakes or climatic warming in alpine mountains play a

12 crucial role in sediment delivery from hillslopes and downslope channels into rivers. Rapid and massive sediment supply

13 to rivers by the debris flows has profoundly influenced the evolution of the alpine landscape. Nonetheless, there is a dearth

14 of knowledge concerning the roles tectonic and climatic factors played in the intensified sediment erosion and transportation.

15 In order to increase our awareness of the mass wasting processes and glacier changes, five debris flows that occurred at the

16 Zelunglung catchment of the eastern syntaxis of the Himalayas since 1950 Assam earthquake are investigated in detail by field

17 surveys and long-term remote sensing interpretation. Long-term seismic and meteorological data indicate that the four events

18 of 1950-1984 were the legacies of the earthquake, and recent warming events drove the 2020 event. The transported sediment

19 volume indexed with a non-vegetated area on the alluvial fan reduced by 91% to a stable low level nearly 40 years after 1950.

20 It is reasonable to hypothesize that tectonic and climatic factors alternately drive the sediment supplies caused by the debris

21 flows. High concentrations of coarse grains, intense erosion, and extreme impact force of the 2020 debris flow raised concerns

22 about the impacts of such excess sediment inputs on the downstream river evolution and infrastructure safety. In regard to the

23 hydrometeorological conditions of the main river, the time to evacuate the transported coarse sediments is approximately two

24 orders of magnitude of the recurrence period of periglacial debris flows.

25

26 1 Introduction

27 Glacier-related hazards are widely developed in alpine regions around the world, such as the Alps, Himalayas, Caucasus,

28 Tianshan, and Andes (Richardson and Reynolds, 2000; Anacona et al., 2015; Shen et al., 2013; Petrakov et al., 2007; Huggel

29 et al., 2004). These hazards, including ice/rock avalanches, periglacial debris flows, glacial lake outburst floods (GLOFs), and

30 dammed lakes, have caused huge economic and human losses in the high mountains and their surrounding area (Yu et al.,

31   2021; Tian et al., 2017; Bajracharya and Mool, 2009; Hu et al., 2019). Earthquakes, geothermal heating, climate warming,

32   rainfall, and meltwater all trigger glacier-related hazards (Huggel, 2004; Haeberli et al., 2014). Especially in the context of

33   climate change (rising temperatures and increased extreme precipitation events), the high-altitude regions such as European

34   mountains, high-mountain Asia, and the Andes are undergoing rapid deglaciation that increases the magnitude and frequency

35   of ice/rock avalanches and low-angle glacier detachments accordingly (Anacona et al., 2015; Krautblatter et al., 2013).

36   In recent years, the Himalayan mountains, which are tectonically active and sensitive to climate change, have experienced

37   many large-magnitude earthquakes or climate-driven disasters. The increased glacier-related disasters have profound

38   hydrogeomorphic and socio-economic impacts on the high-altitude and surrounding regions, including sediment yield and

39   transportation, alpine landscape evolution, river management, food and water security, hydropower utilization, and

40   infrastructure construction (Evans and Clague, 1994; Kääb et al., 2021). For example, on 25 April 2015, a disastrous ice-rock

41   collapse was triggered by the Gorkha earthquake and killed or left missing at least 350 people in the Langtang Valley of central

42   Nepal (Kargel et al., 2016). From 2017 to 2018, several ice-rock avalanches in the Sedongpu catchment of Milin County, Tibet

43   Autonomous Region (TAR), China triggered large-scale glacial debris flow events that blocked the Yarlung Tsangpo River

44   twice (Li et al., 2022; Hu et al., 2019; Jia et al., 2019). On 7 February 2021, about 27×10^6 m^3 of rock and ice collapsed and

45   quickly transformed into a debris flow in Chamoli, Uttarakhand region of India, which killed more than 200 people and

46   severely damaged two hydropower projects (Shugar et al., 2021). These disasters seriously threaten the safety of life and

47   property of local and downstream residents, leading to the challenges of transboundary hazards and international collaboration.

48   When ice-rock avalanches, glacier surges, or GLOFs are accompanied by ice melting, mass mixing, and bed entrainment in

49   the channelized propagation, they often transform into periglacial debris flows. The volume of ice loss and sediment

50   transportation via periglacial debris flows is huge and poses long-term effects on the high mountain environment. The Institute

51   of Mountain Hazards and Environment, Chinese Academy of Sciences (IMHE, CAS) reported that a total volume of 200 Mm^3

52   of sediment transported into an upstream tributary of the Brahmaputra River by periglacial debris flows of the Guxiang

53   catchment in southeastern Tibet from 1953 to 1999 (Wang et al., 2022). The ice-rock avalanches of the Sedongpu in October

54   2018 delivered about 33.2 Mm^3 of sediment into the Yarlung Tsangpo River (Hu et al., 2019). The total mass loss caused by

55   glacier-rock avalanches in Sedongpu between 2014 and 2018 reached > 70 Mm^3 of glacier and rock and > 150 Mm^3 of moraine

56   deposits (Li et al., 2022). Furthermore, after the glacier detachment of the Sedongpu in 2018, a huge volume of ~335 Mm^3 was

57   eroded from its glacier bed and transported into the Yarlung Tsangpo (Kääb and Girod, 2023). Sudden enormous sediment

58   inputs greatly influence sediment transport capacity, knickpoint formation, river water quality, downstream floods, and delta

59   progradation. The 2021 Chamoli event resulted in extremely suspended sediment as 80 times high as the permissible level in

60   the Ganga River, ~900 km from the source (Shugar et al., 2021). Sediment fluxes have increased two- to eight-fold in many

61   glacierized and peri-glacierized basins between the 1950s and 2010s (Zhang et al., 2022a). However, little is known about the

62   roles the extreme hazards play in incrementing sediment erosion, transportation, and the control of the hazards between tectonic

63   and climatic factors.

This paper investigates glacier changes and associated debris flows in the Zelunglung catchment, a tributary of the Yarlung Tsangpo river in southeastern Tibet, since the 1950 Assam earthquake. Four historical periglacial debris flows occurred in this catchment in 1950, 1968, 1972, and 1984 (Zhang, 1992; Zhang and Shen, 2011). The most recent debris-flow event occurred on 10 September 2020, triggered by a small-scale ice-rock avalanche. It is believed that historical earthquakes and ongoing climate warming drive these events. Field surveys were carried out before and after the 2020 event, including three periods of aerial photography on 8 September, 11 September 2020, and December 21, 2022, with DJI Unmanned Aerial Vehicle (UAV). Dynamic process and sediment characteristics of the 2020 event were examined with the details of aerial photos and field measurements. The Zelunglung's glacier and alluviation fan changes were interpreted with high-resolution optical remote sensing images from 1969 to 2022. The non-vegetated area of the alluvial fan was used as an index to reflect the variation of sediment supply caused by the periglacial debris flows. Integrating with historical data of neighboring earthquakes, temperature, and precipitation, we demonstrate the trend of periglacial debris flows in different periods. This case study is helpful for a better understanding of the controlling factors and sediment transportation of periglacial debris flows in High Mountain Asia (HMA).

2 Study area

The Zelunglung catchment (94°56′13.4″E, 29°36′25.6″N) at Zhibai Village in the China's TAR is a tributary on the right bank of the lower Yarlung Tsangpo River, originating from the west side of Namche Barwa massif (7782 m) in the easternmost part of the Himalayas. The main stream flows westward into the Yarlung Tsangpo at an elevation of 2810 m, with a local relief of 4972 m (**Fig. 1a**). It has a drainage area of 41.21 km^2 with a 17.9 km^2 glacier area. High lateral moraines on both sides of the main glacier divide the drainage network into the main channel, south branch, and north branch (**Fig. 1b**). The south branch, with a total length of 9.8 km and an average gradient of 275‰, originates from the southern cliff at an elevation of ~5900 m. Hanging glaciers on the ridge and freeze-thawing in the cold region make the study area prone to ice and rock avalanches (**Fig. 1c**).
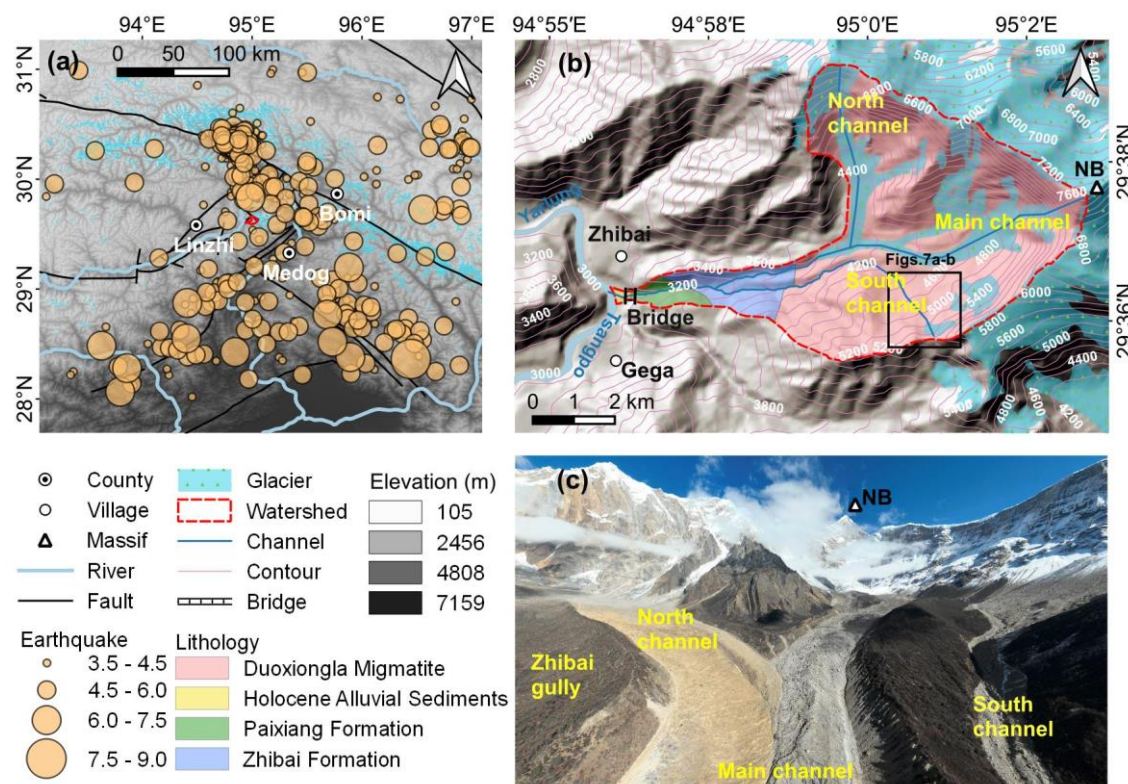
Figure 1: (a) Regional settings and historical earthquakes of southeastern Tibet. (b) Topographic and geological maps of the Zelunglung catchment (the lithology refers to (Zhang and Shen, 2011)). (c) Aerial photo of the Zelunglung glacier and channels on December 21, 2022 (NB denotes the Namche Barwa massif).

The regional tectonic units are the Lhasa terrane, the Indus-Yarlung Tsangpo suture, and the eastern syntaxis of the Himalayas from north to south (Hu et al., 2021). The catchment lies in the eastern syntaxis, which is uplifting at a rate of 5-10 mm/a (Ding et al., 2001). The exposed stratum in the Zelunglung is known as the Namche Barwa Group complex, which is composed of Duoxiongla migmatite, Zhibai group, and Paixiang group gneiss. The Quaternary deposits consist of Holocene alluvium at its outlet, thick layers of glacial till, and glacio-fluvial accumulation, especially hundreds of meters of huge thick moraine layers with large boulders accumulated on both sides of the main channel (**Fig. 1b**) (Han and Feng, 2018; Zhang and Shen, 2011). Many active faults are distributed around the study area, such as the Aniqiao-Medog Fault to the east, which is considered the seismogenic fault of the 1950 Ms=8.5 Assam earthquake, NW-SE Xixingla fault that is the seismogenic fault of the 2017 Ms=6.9 Milin earthquake, and Daduka Fault across the Zelunglung downstream (Hu et al., 2019). Neotectonic movement makes this area highly susceptible to intense and frequent earthquakes.

This catchment lies in the rain shadow area of Mt. Namche Barwa, and its precipitation is controlled by the Indian Ocean's humid monsoon through the Yarlung Tsangpo Gorge. The climate has a strong vertical difference: semi-humid climate zone beneath 3200 m, cold temperate climate zone between 3200-4000 m, and cold climate zone above 4000 m. According to the

103 data recorded at the Linzhi meteorological station 46.2 km west of the Zelunglung, the annual air temperature with a mean

104 value of 9.8 °C increases at an average rate of 0.36 °C/10a from 2000 to 2021, which is much higher than the global average

105 (Chen et al., 2015). Meanwhile, the annual precipitation ranges from 514 mm to 972 mm and increases at an average rate of

106 0.65 mm/10a (**Fig. 2**).

107
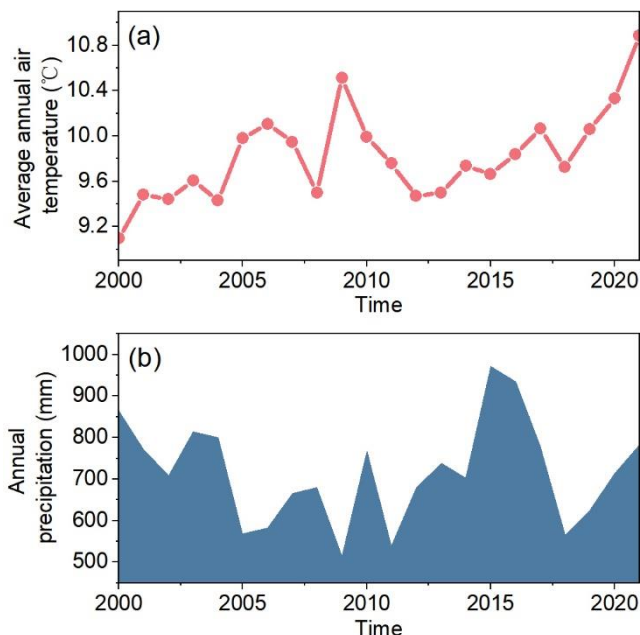
Figure 2: Annual temperature and precipitation data from 2000 to 2021 at Linzhi Meteorological Station. (Data source:
https://www.ncei.noaa.gov/maps/annual/).

110 **3 Data and methodology**

111 **3.1 Data sources**

112 We collected a total of 30 different remote sensing images from various sources dating back to 1969, with resolutions ranging

113 from 1m to 15m (**Table 1**). Images before 1982 were sourced from the Keyhole reconnaissance satellites

114 (https://earthexplorer.usgs.gov/), originally serving as the primary data source for the United States Department of Defence

115 and intelligence agencies for Earth imaging. These high-resolution images provide valuable visible data in the era without

116 commercial satellite imagery. Images from 1988 to 2007 originated from the Centre National d'Études Spatiales (CNES)

117 SPOT series data (https://regards.cnes.fr/user/swh/modules/60). Images from 2009 are sourced from the RapidEye series and

118 Planet satellites (https://account.planet.com/), which are known for their short revisit periods and high resolution. To

119 comprehensively document the historical debris flow activity in Zelunglung, we diligently chose images captured after every

120 rainy season (October to December) whenever feasible. Due to high cloud cover in the study area and limited availability of

5

121 image resources, we substituted images from the following year before May for specific periods with significant image data
122 gaps (e.g., before 2000) for those of the missing year (Li et al., 2017). Although the Landsat satellite series may offer more
123 continuous observational records, their relatively coarse resolution makes them unsuitable for our study area.

124 **Table 1: Data sources of the satellite images used in this study.**

No.	Date	Data sources	Resolution (m)
1	1969	Keyhole	5
2	1972/2/28	Keyhole	1
3	1973/3/26	Keyhole	1
4	1975/12/21	Keyhole	4
5	1979/4/10	Keyhole	1
6	1982/10/15	Keyhole	1
7	1988/2/20	Spot1	15
8	1989/12/1	Spot1	15
9	1990/12/21	Spot2	12
10	1991/11/25	Spot3	12
11	2000/11/17	Spot4	10
12	2002/12/5	Spot5	6
13	2004/12/28	Spot5	6
14	2005/10/10	Spot5	6
15	2006/12/21	Spot5	6
16	2007/11/29	Spot5	6
17	2009/12/22	RapidEye	5
18	2010/12/15	RapidEye	5
19	2011/11/23	RapidEye	5
20	2012/12/15	RapidEye	5
21	2013/12/7	RapidEye	5
22	2014/12/13	RapidEye	5
23	2015/12/6	RapidEye	5
24	2016/12/13	Planet	3
25	2017/12/11	Planet	5
26	2018/12/13	Planet	3
27	2019/12/7	Planet	3
28	2020/12/10	Planet	3

| 29 | 2021/12/12 | Planet | 3 |
| 30 | 2022/12/10 | Planet | 3 |

3.2 Field surveys

We conducted three field surveys in the Zelunglung between 2020 - 2022. During the first survey, we conducted two aerial drone photography works on September 9 and 11, 2020, using DJI MAVIC 2. High-resolution orthoimages and digital surface models (DSM) for the channel and fan areas of Zelunglung were generated from the aerial photos. Additionally, we measured downstream channel cross-sectional morphology, debris flow particle characteristics, and the extent of damage to the Zhibai Bridge. In 2021, we conducted a follow-up field survey at the same site. A full 3D view of the Zelunglung was captured with an unmanned aerial vehicle (UAV) in the third survey on December 21, 2022, a sunny winter day (**Fig. 1c**).

3.3 Methodology

The inundation of debris flow on the alluvial fan often destroys vegetation cover and causes the affected area to desertify in a few years. Generally, the non-vegetated area (NVA) depends on the flow magnitude. So, the non-vegetated area of the alluvial fan shortly after a glacial debris flow can serve as a proxy of the volume of transported sediment. It should be noted that distinguishing fresh debris flow deposits on an alluvial fan from pre-existing exposed surfaces in the surrounding area is challenging in satellite images due to minimal color differences. Additionally, due to the slow vegetation recovery rate in high-altitude regions, our interpretation area likely includes exposed areas one year or several years before an event. Therefore, the NVA has some uncertainties in representing the real magnitude of the debris flows.

We employed a visual interpretation approach to delineate non-vegetated areas within the Zelunglung's alluvial fan. Identifying the non-vegetated area is primarily based on differences in color, hue, texture, and shading between vegetated and unvegetated regions. The Keyhole black and white photos and the SPOT single-band black and white images show distinct tonal differences between vegetated and unvegetated areas. In the true-color images obtained from RapidEye and Planet, the boundaries of NVAs are highly conspicuous. The Zelunglung interpretation zone is limited to the region between the two adjacent confluences of its upstream and downstream catchments with the main river.

Due to potential misalignment between remote sensing images from different sources, image matching is performed before manual delineation of the non-vegetated areas (Cui et al., 2022). To eliminate the errors of geospatial locations of the images from different sources, we used the 2020 Planet image as the reference image and selected ground control points with clear markers on this image, such as road junctions, rivers, and typical topographic points. Third-order polynomial transformation is applied to match the images from other sources accurately with the 2020 image, ensuring a positional error of less than 20 m relative to the reference image. The original Keyhole images without geographical coordinates and projection system information are georeferenced with the 2020 Planet image with the ground control points. We assume that the visual interpretation error of non-vegetated areas is approximately one grid cell on either side of the boundary. Moreover, we verified

154 the interpretation results of the remote sensing images with the UAV orthoimages. Utilizing post-event drone orthoimages

155 captured in 2020, we visually interpreted the distribution of particles from the downstream channel to the depositional fan.

156 High resolution and accurate color representation of the drone aerial images enable us to reliably identify coarse particles (>50

157 cm). The interpretation results were compared with measurements obtained with a caliper during the 2022 field survey.

4 Glacier changes and debris-flow events

4.1 Rapid glacier changes

160 The Zelunglung has experienced at least three glaciations in the Last Glacial Maximum (LGM), Neoglaciation, and Late

161 Holocene (Hu et al., 2020). The LGM moraine extended into the Yarlung Tsangpo and dammed the river (David et al., 2004;

162 Huang et al., 2014; Zhu et al., 2012; Liu et al., 2006). The glacier surges/debris flows - dammed lake - outburst flood disaster

163 events since the last glacial period also had an important impact on the landform and paleogeographical environment of the

164 Yarlung Tsangpo Valley (Wang et al., 2021).

165 The modern glaciers in this area are strongly influenced by the Indian monsoon and are highly sensitive to climate change.

166 Hence, the Zelunglung glacier has advanced and retreated many times since the last century. The high instability and rapid

167 changes of the glacier result in several glacier surges or calving events. As shown in Fig. 3, the glacier snout was 3500 m a.s.l

168 in 1926 (Ward, 1926). Since the 1950s, the Zelunglung glacier has experienced three surges or rapid advances (Zhang, 1985,

169 1992). The first surge occurred on August 15, 1950. Following the 1950 Assam earthquake, the terminus of Zelunglung Glacier

170 advanced from 3650 m a.s.l to the Yarlung Tsangpo at 2810 m a.s.l with a horizontal displacement of up to 4.5 km. This event

171 destroyed the Zhibai Village completely at the mouth of the Zhibai gully, killed 98 people, and formed an ice dam as high as

172 tens of meters in the main river. The second surge occurred one afternoon in August or September of 1968 (July 1968, Tibetan

173 calendar) when it was sunny (Zhang, 1992, 1985). The advance also resulted in a temporary ice dam in the Yarlung Tsangpo

174 and deposited a glacial boulder of 4.0×5.0×5.5 m upstream of the dam (Zhang, 1985). It is worth noting that the position of

175 the ice tongue before the second glacier surge has returned to the position before the first surge (3650 m a.s.l), and the highest

176 speed of the two glacier surges was up to 1.5 km/d. After the second surge, the main glacier split into 6 segments due to

177 differential ablation, and the terminus of the lowest segment of the glacier was at 2950 m a.s.l. The terminus of the lowest

178 segment was about 2980 m a.s.l in 1969 as shown by the Corona reconnaissance satellite images (Kääb et al., 2021). The

179 terminus of the lowest part of the glacier had probably been at 2950 m a.s.l before 13 April 1984 when an ice mass of 80000

180 m^3 detached at 3700 m a.s.l and traveled horizontally 150 m (Zhang, 1992). After that, no glacier surges or detachments were

181 recorded, but small-scale mountain torrent or debris flows occurred almost yearly (Zhang and Shen, 2011). At present, the

182 glacier terminus is about 3770 m a.s.l.
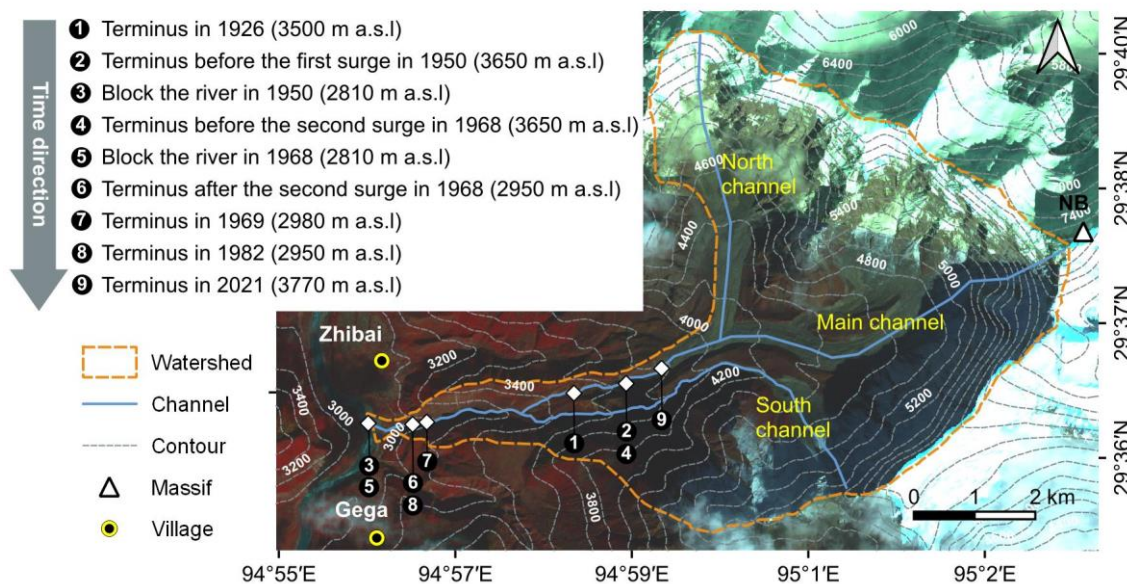
Figure 3: Variations of the Zelunglung main glacier terminus from 1926 to 2021. (The base image is taken from Planet satellite).

4.2 Multi-periodic glacial debris flows

Glacier surges or ice-rock avalanches can be transformed into debris flows that deliver massive amounts of sediment into the river or deposit on the alluvial fan. Four large-magnitude debris flows were triggered by the glacier instability events in 1950, 1968, 1973, and 1984 (Zhang, 1992; Hu et al., 2020). From the 1972 and 1973 images, it is observed that fresh debris deposits inundated the north part of the fan and did not go beyond the 1968 accumulation zone (**Fig. 4**). The same lobes and deposition boundary indicate that the so-called 1973 event mentioned by Peng et al. (2022) likely happened in 1972. The magnitude of the 1950 event is perhaps more significant than that of the 1968 event. According to Zhang (1992), the detached glacier in 1950 climbed over the ~80 meters lateral moraine on the north at an elevation 4000 m and traveled downstream along the Zhibai gully (**Fig. 1c and Fig. 5**). Based on the erosional scar photo on the lateral moraine (Zhang, 1992) and the 2022 UAV photo, the residual depositional area of the 1950 event in the upstream gully is ~ 65,000 m^2 (Fig. 5). Although the glacier detachment happened in Zelunglung in 1950, most of the sediment deposited in the Zhibai channel and its alluvial fan. Fine sediment from the catchment can be quickly transported downstream by river flows, but most coarse sediment is still left on the bank or the alluvial fans.
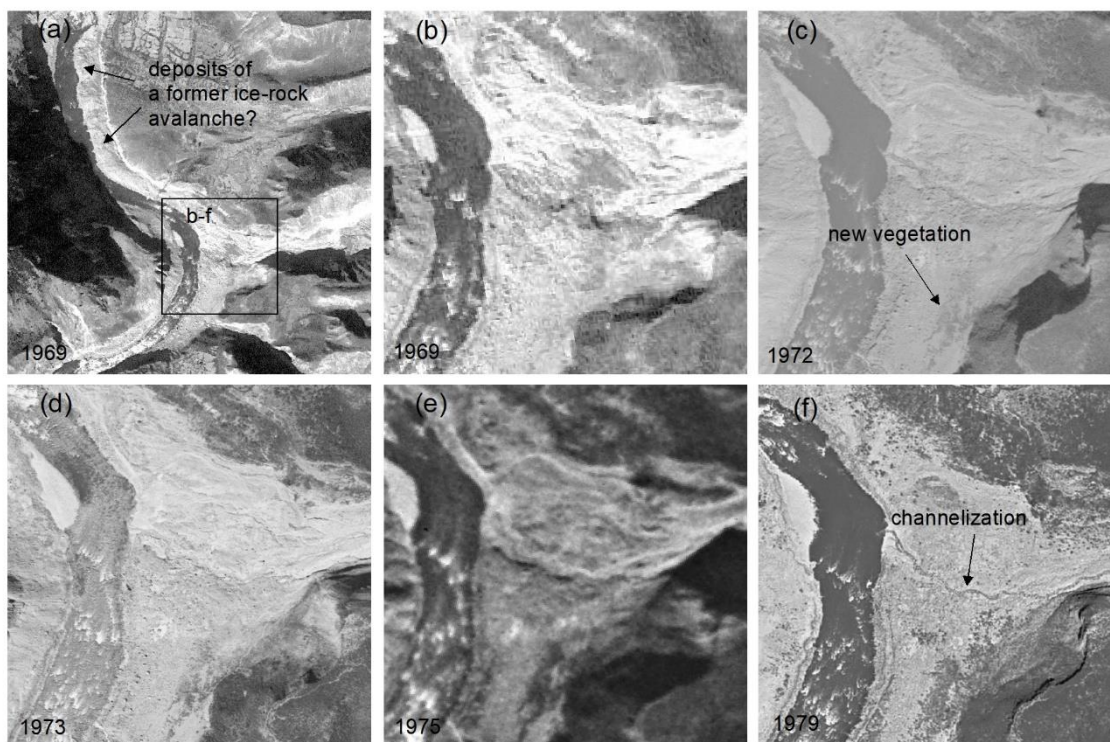
9

Figure 4: Variations of the Zelunglung alluvial fan during 1969 – 1979. The images are taken from Keyhole reconnaissance satellites (https://earthexplorer.usgs.gov/).

There are two terraces on the banks of the main river along the confluences of the Zelunglung ravine and Zhibai gully (**Fig. 6a**). T1 and T2 terraces are ~10 m and ~ 150 m above the river level, respectively (**Fig. 6b**). The 1950 and 1968 events completely dammed the Yarlung Tsangpo (Zhang, 1992). Compared with the 1969 Keyhole image (**Fig. 4a**), it is likely that the T1 terrace is the residual dam of the 1968 event. The debris flows in the 1950 glacier surge event eroded the T2 terrace, which implies that the T2 terrace formed before 1950. The residual inundation area of the 1950 event is ~0.78 km^2 (**Fig. 6a**). If the magnitude is proportional to the inundation area, the flow magnitude of the 1950 event could be larger than that of the 1968 event.

Figure 5: Aerial photo of the Zelunglung main channel on December 21, 2022, and the old deposits in Zhibai gully left by the 1950 event (the camera faces to downstream, and the dashed rectangle indicates the location of Figure 6b).


Figure 6: Two terraces on the banks of the main river. (a) Century Space's satellite image on 9 February 2021. (b) Picture of the terraces on the opposite bank of the Zelunglung taken on 8 September 2020.

214   An ice-rock avalanche triggered the recently documented glacial debris flow on Sep. 10, 2020. The 2020 ice-rock avalanche

215   initiated on the top ridge of the south branch at an elevation of 5500 m. The scar area of initiated ice and rock was 1.35×10^4

216   m^2 on the upper cliff (**Figs. 7a-b**). The initiated volume is estimated to be 7.0×10^4 m^3 by using the bedrock landslide area-

217   volume empirical relationship ($V = \alpha A^\gamma$; $\alpha = 0.186, \gamma = 1.35$) (Larsen et al., 2010). In the Google image on December 4,

218   2017 (**Fig. 7-c2**), it can be seen that there is a protruding rock mass on the cliff below the unstable ice-rock block. The rock

219   mass develops many lateral cracks, and the top is covered with fresh, weathered materials, indicating freezing severe

220   weathering. The fallen ice-rock block partially disintegrated and impacted colluvial deposits on steep hillslope below the cliff

221   at elevations 4570–4800 m, forming a muddy fresh area of 0.134 km^2 (**Fig. 7b**). This area is often covered by snow and ice,

222   and the ice-snow melting water easily infiltrates into the debris-ice mixtures. Once the slope material was entrained into the

223   mass flow, such a nearly saturated mixture could quickly turn into a debris flow. Peng et al. (2022) estimated a debris loss of

224   1.14 Mm^3 in the scarp area except for the initiated ice and rock. But they mistake the hillslope below the cliff as the source

225   area of the event. It is noted that there is an ice-rock residual of ~ 7.14×10^3 m^2 left under the cliff (**Fig. 7-b3**). That means the

226   volume of the debris mass flowed downward into the south channel should include half of the initiated ice-rock mass and the

227   debris loss of 1.14 Mm^3. The entrained volume is at least 16 times the initiated volume.
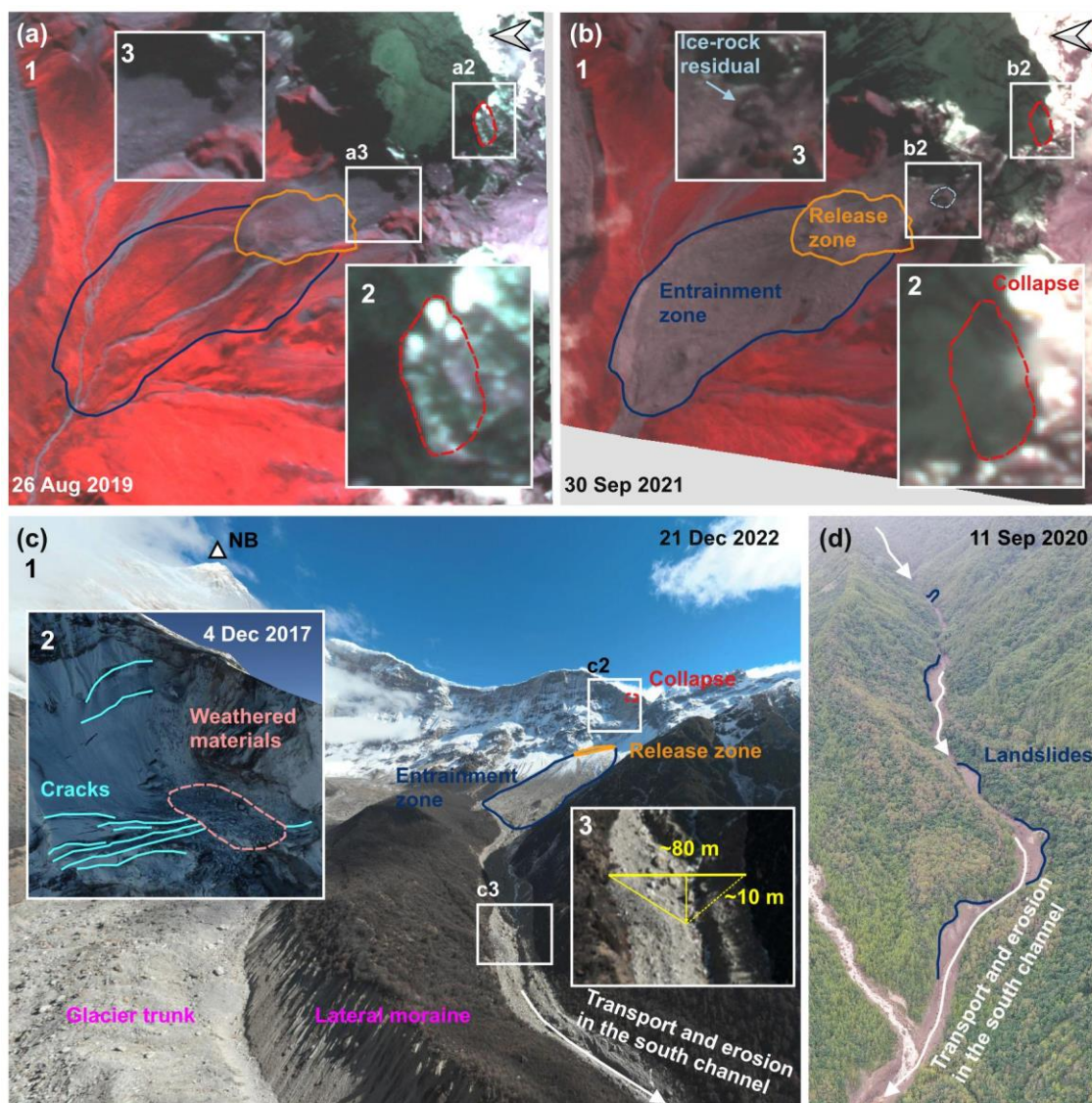
Figure 7: The initiation and propagation of the "9.10" Zelunglung periglacial glacier debris flow. (a) The planet image of the initiation area before the event. (a2) enlarged region over the pre-collapse site. (a3) Enlarge the region over the hillslope before the collapse. (b) The planet image of the initiation area after the event. (b2) enlarged region over the post-collapse site. (b3) enlarged region over the hillslope after the collapse. (the base images in a-b © 2024 Planet Labs PBC) (c) An aerial photo of the source area and the south channel on 21 December 2022 was taken by the UAV. (c2) Google Earth imagery of the initiation area on 2 December 2017 (the base image ©Google Earth). (c3) The region was enlarged over the south channel on 21 December 2022. (d) An aerial photo of the downstream channel on 11 September 2020 was taken by the UAV.

When the debris flows travelled downstream, parts of old channel sediment and lateral moraines were eroded while some of the flow mass was deposited on the banks. The flows also triggered many small landslides on both banks of the middle stream (**Fig. 7d**). The blockage by large boulders and the induced landslides on the narrow channel may enlarge the magnitude of the debris flows in the end (**Fig. 7d**) (Cui et al., 2013; Liu et al., 2020). The UAV photo shows the influx of debris flows that

240 transformed from the entrained sediment and melting water exceeded the average water level of the south channel. The flow

241 cross-section is ~ 80 m wide at the top and ~ 10 m high in the thalweg based on the UAV photo and OpenCycle topographic

242 map (**Fig. 7-c3**). The peak discharge and frontal flow velocity reached 4700 m^3/s and 11.4 m/s at the outlet (Peng et al., 2022).

243 According to the description of local villagers, the first debris flow surge arrived at Zelunglung's mouth at about 5:00 pm on

244 September 10, and the second larger one arrived about one hour later. Two ice-rock avalanches with different volumes probably

245 happened on the ridge and were the corresponding trigger of the downstream debris-flow surges. But it is more likely that

246 there was only one ice-rock avalanche during the event, but a synchronization of the ice-rock impacts in the scarp area, and

247 the channel blockage caused two debris-flow surges.

4.3 Sediment characteristics of the 2020 event

4.3.1 Difference between the initiation and the downstream areas

250 Periglacial debris flows can transport rocks or boulders not only in midstream steep channels but also in gentle downstream

251 channels or alluvial fans. The sediment transportation capacity of the flows depends on flow hydrodynamics, grain composition,

252 and topographic conditions. The 2020 Zelunglung event provides first-hand information for examining such sediment

253 characteristics of the flows. Next, we present on-site data such as the size distribution of coarse grains, their impact, and erosion.

254 The field evidence shows some features of periglacial debris-flow transportation that differ from fluvial transport.

255 There is a big difference between the sediment composition in the source and depositional areas. The initiated ice-rock debris

256 and colluvial deposits on steep hillslopes consisted of angular rocks of various sizes. However, we observe that the deposits in

257 the downstream areas are sub-rounded stones, and the downstream banks and channel bed are composed of sands and boulders

258 up to several meters in diameter (**Fig. 8**). That means most of the angular rocks resided in the upslope or upstream channel and

259 did not move downward. The angularity of the fragmented rocks reduced their mobility, and the attenuated overland flow had

260 less transport capacity. The large sub-rounded or sub-angular boulders in the lower reaches came from the middle of the

261 downstream reaches. We guess that grain segregation happened initially, and only fine parts of the ice-rock mass and melting

262 water traveled downward the midstream. The resident angular rocks would be rounded gradually by the periglacial stream and

263 transported downward by the subsequent floods or debris flows. The transportation mode of coarse grains is a kind of "Relay-

264 race style", one event by one event.

265 Numerous boulders were on the channel and banks before the 2020 event, as seen from the aerial photo on 9 September 2020

266 (**Fig. 8a**). The in situ boulders were mobilized by the upstream flows and reorganized spatially. The boulders were prone to

267 move together on the flat banks such as a flat storage yard near the bridge and the fan middle (**Fig. 8b**). The slope and flow

268 depth are critical for the boulder's transport. Interstitial slurry among the boulders could separate from the boulders when the

269 debris flows moved on a gentle slope or spread over an open fan (**Fig. 8c**). The interstitial slurry provided buoyancy for the

270 boulders and reduced resistance between them and the bed. Once there was no interstitial slurry, the boulders quickly stopped.
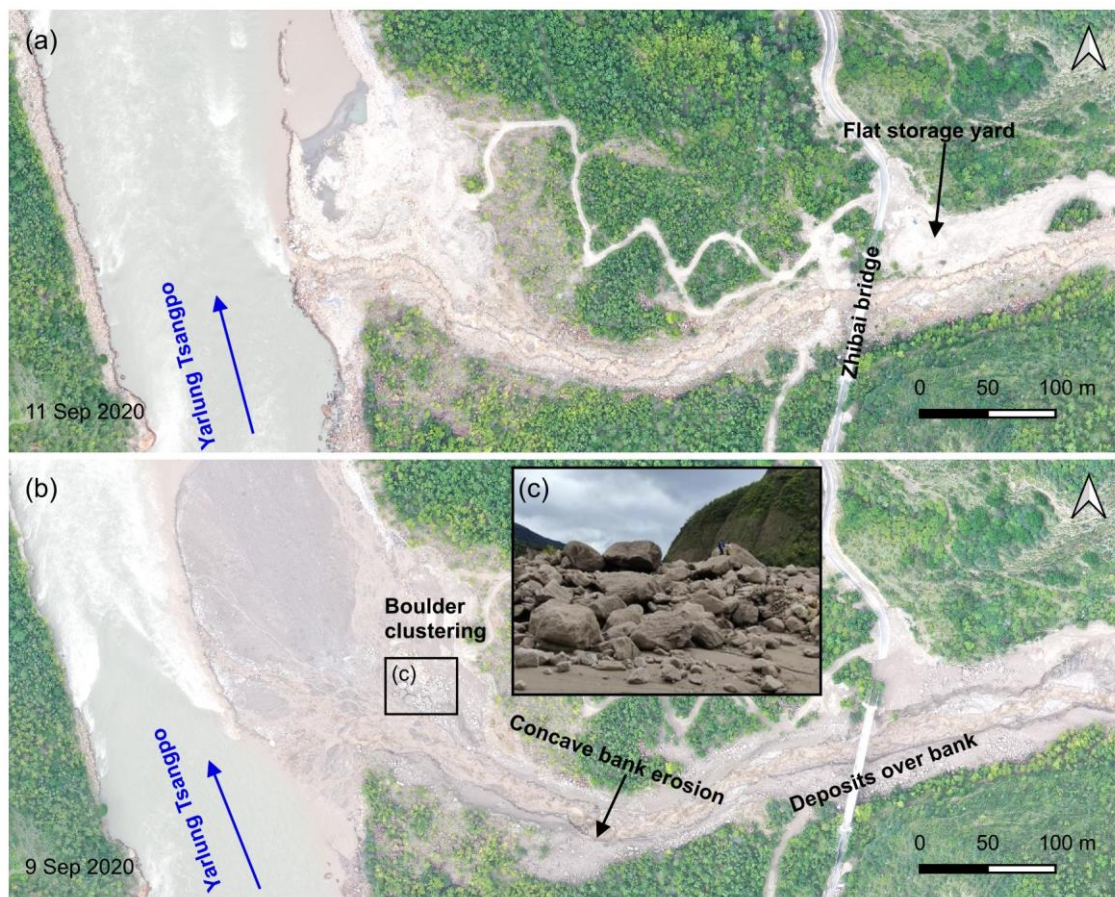
Figure 8: Comparison of pre-and post-event aerial photos on the downstream channel and alluvial fan. (a) the UAV photo on 9 September 2020; (b) the UAV photo on 11 September 2020; (c) On-site picture of the boulder clustering on 11 September 2020 (the man's height is 1.7 m).

4.3.2 Grain-size distribution of coarse particles > 50 cm

In the downstream channel, with an average gradient of 13.8%, a relatively high velocity (11.4 m/s) enabled the flows to mobilize boulders of 5.0 meters in diameter (Costa, 1983). An 1125 m long straight reach from the first bend upstream of the bridge to the edge of the alluvial fan was chosen. Coarse particles > 50 cm on the deposition surface were visually interpreted from the orthophotos with a resolution of 0.17 m on September 11, 2020, after the debris-flow event. The long axis of the equivalent ellipse of these particles represents the particle size. Due to the limitation of resolution, only coarse particles with a long axis larger than 50 cm were counted (**Fig. 9**). A total of 3943 coarse particles were identified and divided into four size ranges of 50-100, 100-300, 300-600 and >600 cm. Spatial statistics of these particles were made every 25 m along the central flow line, and then 45 segments were divided.
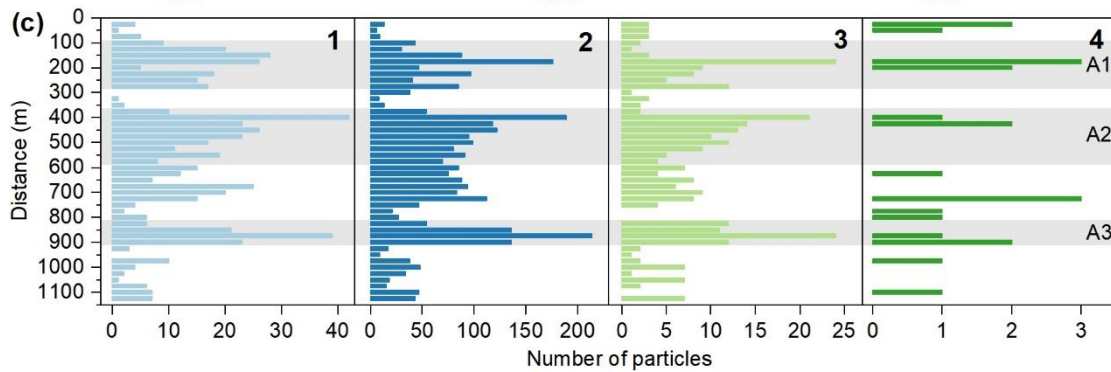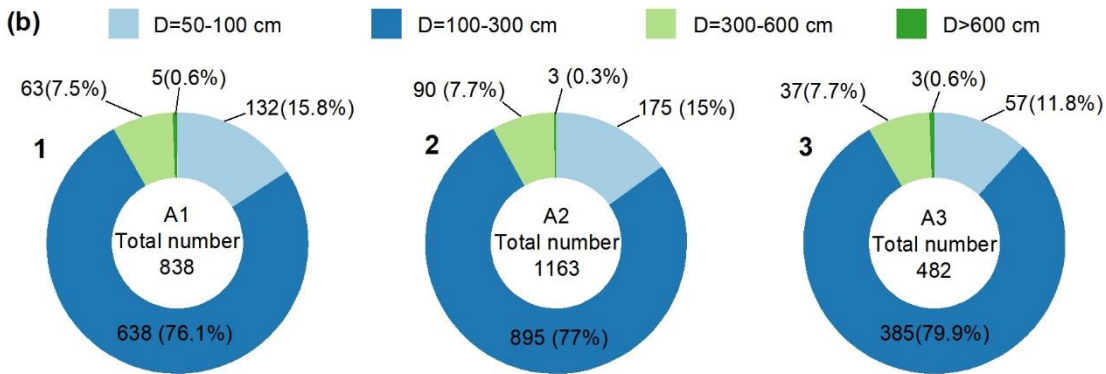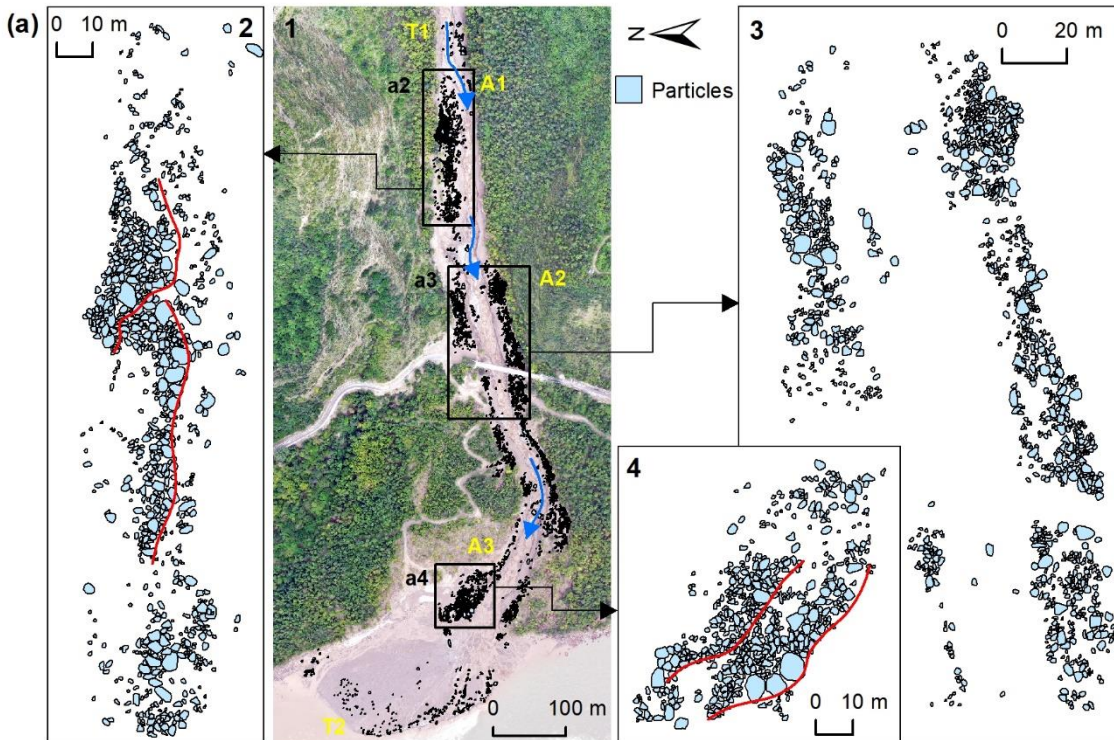
15

Figure 9: Distribution of the coarse particles on the sediment surface. (a) The distribution of coarse particles along the channel and alluvial fan. T1 and T2 are the start and end points, respectively. A1-A3 are the three main deposition sites. The blue arrow is the direction of the debris flows. The bottom image is an orthographic image taken by a drone on September 10, 2020. The locations of the enlarged regions (a2)-(a4) are shown as black boxes. (a2)-(a4) enlarged region over the three main deposition sites A1-A3. Panels (b1)-(b3) show the counts of four groups of the particles in the three main deposition sites A1-A3. Panels (c1)-(c4) show the counts of four groups of the particles in the 45 segments. Particles with diameters of 50-100 cm, 100-300 cm, 300-600 cm, and particles larger than 600 cm in panels b-c are shown in light blue, blue, light green, and green.

63% of the particles are concentrated in three zones A1, A2, A3 (**Figs. 9a-b**). The three zones are gentle banks or floodplains. The large stones easily slowed down when the flow depth and the velocity decreased on the edges of the debris flows. The composition of the particles in A1-A3 exhibits similar grain size distribution (**Fig. 9b**). The size of the most numerous particles is between 100 and 300 cm. The stones with the size > 600 cm are the least. The number of particles with 100-300 cm size accounts for 77.4% of the total. Likewise, the particles with sizes of 50-100 cm, 300-600 cm, and >600 cm, accounted for 14.3%, 7.7%, and 0.6% of the total, respectively. If the particle volume is estimated with the equivalent ellipsoid volume, i.e. $V = (4\pi abc) / 3$ (where a is major radius, b is short radius, c is polar radius and equal to b), the two groups of particles with the sizes of 100-300 cm and 300-600 cm have the largest volume.

The spatial distribution of these particles in the 45 segments is shown in **Figure 9c**. The same four size ranges are used (50-100 cm, 100-300 cm, 300-600 cm, and > 600 cm). The particles with the first three sizes have three peaks in A1, A2, and A3 (**Fig. 9c**). The first peak is located on the right bank highland of A1. When the debris flows moved to A1, the flow depth was far higher than the channel depth. Many coarse particles were left on the highland. The second peak is located on both channel sides above Zhibai Bridge. When the debris flow enters the bend at a high speed, a large velocity difference will be generated on the concave-convex bank, i.e., the super-elevation effect (Chen et al., 2009). The debris flows produced the super-elevation effect when they moved to A2, a partially curved channel. Then, some coarse particles overflowed the channel and deposited on the A2 banks. The third peak is at the top of the alluvial fan. When the debris flows moved out the mouth and had no boundary constraint, the other coarse particles gradually deposited from the fan top to the fan edge due to loss of kinetic energy. In the A1 highland, the particle size decreased toward the outer edge of the channel (**Fig. 9-a2**), while the coarse particles in A2 were poorly sorted (**Fig. 9-a3**). In A3, the coarse particles on the surface show the parallel superposition of two depositional units, and the particle size of each depositional unit generally decreases toward the outer edge of the channel (**Fig. 9-a4**). It reflects the gradual accumulation of multiple debris-flow surges (Major, 1998; Sohn, 2000). The two depositional units may correspond to the two successive debris flow surges in Zelunglung at 5:00 pm and 6:00 pm.

4.3.3 Impact and erosion

Debris flows usually have steep coarse-grained surge fronts (snouts) and inter-surge watery flows (Mccoy et al., 2013; Yan et al., 2023). The periglacial debris flows in Zelunglung had similar spatial compositions. The granular flows (coarse-grained snouts) at the fronts exerted a powerful impact on obstacles, and the inter-surge watery flows or water-rich tails with relatively low sediment concentration played critical roles in erosion. The Zelunglung debris flows had a very high content of coarse

319   particles and wide distribution. The impact of the coarse particles witnessed by the damages of the Zhibai bridge, a 100m long

320   cable bridge with a steel frame (**Fig. 10a**). The foundation of the bridge was exposed by the strong erosion capacity of the

321   debris flows (**Fig. 10b**). The middle steel frame was intensely impacted by run-up boulders and highly deformed (**Fig. 10c**).

322   The concrete bridge body displaced 16 cm in vertical direction and 36 cm in horizontal direction (**Figs. 10d and e**). The

323   velocity of the largest boulder with a size of 9.9 m was 12.6 m s^{-1}, and the impact force of the largest boulder was estimated to

324   be 3.64×10^6 kN. The velocity of the debris flow at the selected cross section near the Zhibai bridge was 9.65 m/s, the peak

325   value of debris-flow runoff was 1743.4 m^3/s（**Fig. 11**）(Li et al., 2023) .
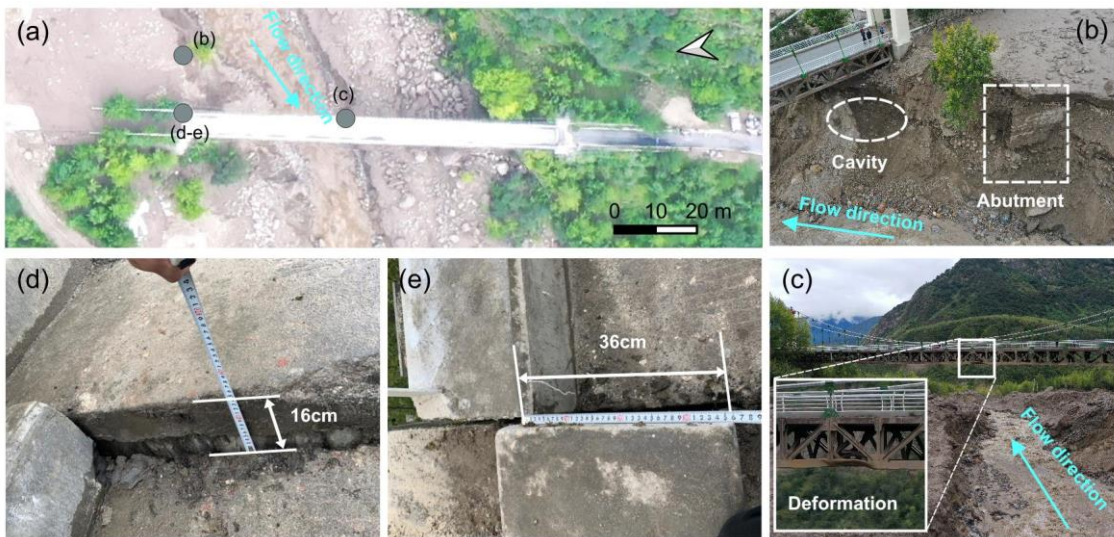
Figure 10: Damages to the Zhibai Bridge caused by debris flows (photos taken on 11 Sep 2020). (a) The overview of Zhibai Bridge taken by UAV and the locations shown in photographs (b)-(e) taken with handheld cameras are shown in gray circles. (b) The photo of the damaged bridge foundation. (c) The photo of the damaged steel frame. (d) Photo of on-site measurements of the vertical displacement of the bridge. (e) Photo of on-site measurements of the horizontal displacement of the bridge.
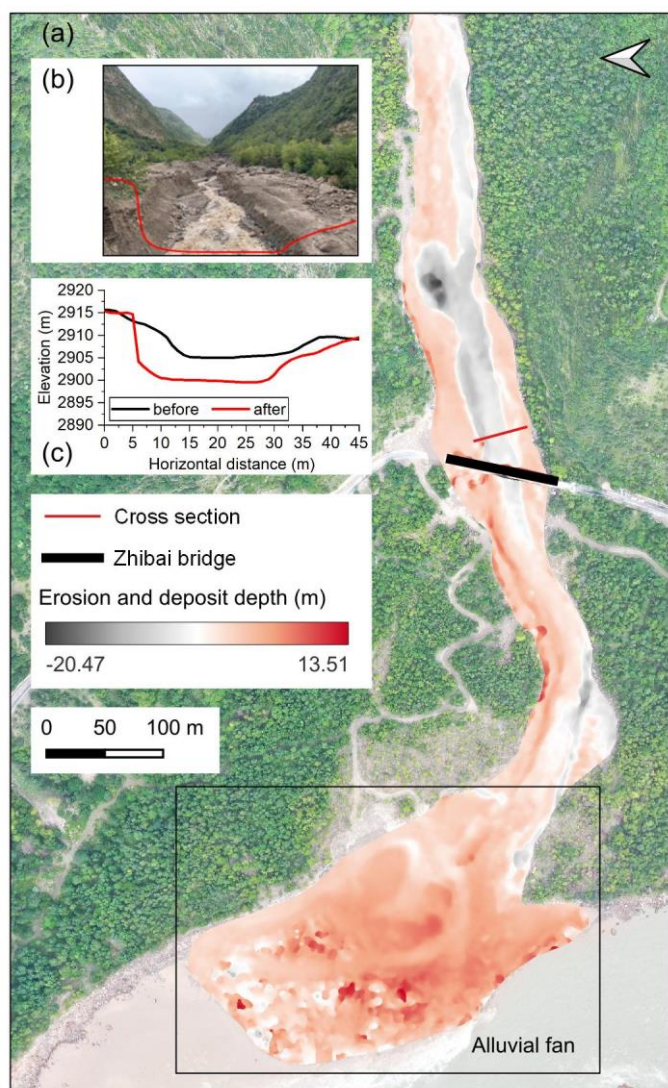
Figure 11: Geomorphic changes of the channel and alluvial fan after the debris flows of 2020. (a) Erosion and deposit depth caused by the debris flows. The base map is taken by UAV on 10 Sep 2020. (b) Photo of the channel after the debris flows. The red line represents the cross-section next to the Zhibai Bridge (photo taken on 11 Sep 2020). (c) Cross-sections before (black) and after (red) the debris flows.

The watery flows were some kinds of dilute flows or hyper-concentrated flows. A vibrating sieve measured one sample taken from the debris-flow deposits with the size < 100 mm. The concentration of sediment finer than 0.075 mm is low, only 3.8% of the whole sample's mass (**Fig. 12**). D50 and D90 of the sample are 8.3 mm and 62.9 mm, respectively, as linearly interpolated from the sieve-measured data. The field evidence shows that the debris flows strongly eroded the downstream channel. Comparing the drone-obtained Digital Surface Model (DSM) data before and after the 9.10 event, the maximum erosive depth was up to 20.47 m (**Fig. 11a**). Peng et al. (2022) numerically simulated the final erosion and deposition along

19

342 the flow path. The maximum erosion depth was 7.41 m at the beginning of the downstream channel. We think the simulation

343 underestimates the erosion depth because the final erosion accumulates several erosive watery flows. Lateral erosion happened

344 nearly along the whole downstream channel. The channel width increased from 17 m to 33 m at 70 m upstream of the bridge.

345 The lateral erosion exposed the bridge foundation, and a cavity formed below the pier (**Fig. 10b**). Concave bank erosion

346 widened the channel by 14 m downstream. Based on the DSMs, we estimated that at least $12.8 \times 10^4 \, \text{m}^3$ of debris was transported

347 out of the catchment (Fig. 11a). However, compared with the study of Peng et al. (2022), the true volume may be seriously

348 underestimated because part of the sediment may be submerged or carried away by the Yarlung Tsangpo River.
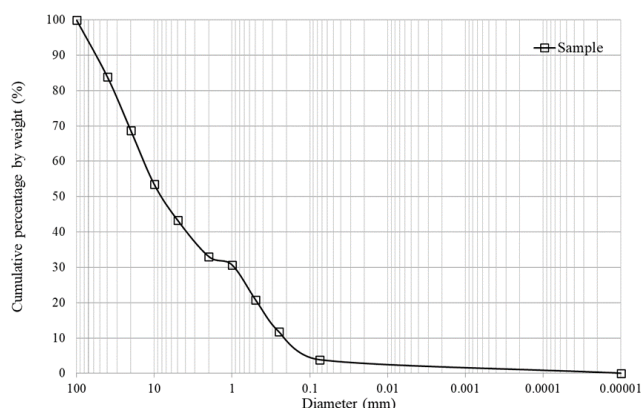
349

350 **Figure 12: Cumulative grain size distribution of the on-site sample with size < 100 mm.**

## 5 Multi-periodic Sedimentation in the confluence

352 Multi-periodic periglacial debris flows are strongly related to variations in the NVA of the alluvial fan. In practice, the NVA

353 includes a fixed part of the area inundated by the river and then is larger than the debris-flow depositional or flooded area (**Fig.**

354 **13**). Technically, the NVA caused by the main river cannot be completely excluded from the total area. However, the river

355 bank line was fixed from the 1980s to the 2010s when no periglacial debris flows happened (**Figs. 13b and c**). So, it is

356 reasonably assumed that the variation of the river water level has no significant influence on the NVA's change, and it

357 represents the volume trend of the sediment transported by the debris flows.

358 From the Keyhole satellite image in 1969, the deposited debris from the 1968 event resided on the confluence and covered a

359 2.5 km downstream reach of the Yarlung Tsangpo River from the junction (**Fig. 4a**) (Kääb et al., 2021). During 1969 – 1979,

360 the area of the accumulated fan kept at about 0.28 km². The 1979 image shows vegetation gradually developed from the edge

361 of the accumulation fan. A new channel developed along the 1972 deposition boundary across the middle of the fan (**Fig. 4f**).

362 Since then, the area without vegetation cover has reduced to 0.048 km2 in 2005 and kept a slight fluctuation from 1985 to

363 2005. It indicates that only rainfall-induced small-scale flash floods or debris flows occurred during 1985-2005, which is

364 confirmed by Zhang and Shen (2011). The NVA increased slowly, with a slight variation from 2005-2019. In 2020, the NVA

365 abruptly increased to 0.112 km² due to the ice-rock avalanche that happened on September 10 (**Fig. 13**). The expansion of

366 NVA in 2020 demonstrates it is the most enormous debris flow event in the Zelunglung since 1972. At the same time, the river

367 channel narrowed down by more than 60 meters compared to before. The multi-periodic sedimentation in the Zelunlung and

368 Zhibai fans leads to rapids in this reach, forming a knickpoint before the river enters the Yarlung Grand Canyon.
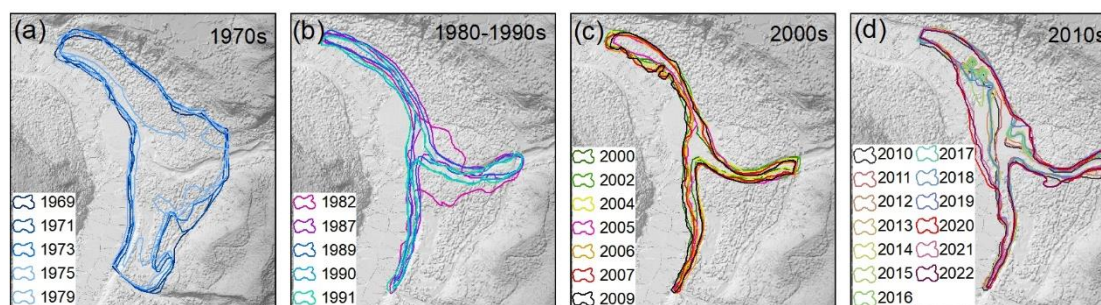

370 **Figure 13: Evolution of the non-vegetated area in the Zelunglung alluvial fan from 1969 to 2022.**

371 The data of seismic events since 1940 are collected from the United States Geological Survey (USGS) National Earthquake

372 Center (NEIC) (https://earthquake.usgs.gov/earthquakes/search/) (**Fig. 14a**). It is observed that the four events in the

373 Zelunglung in 1950, 1968, 1984, and 2020 were preceded by significant seismic activity. Nearly 30 earthquakes with $Mw \geq$

374 4.5 occurred within one year before the 2020 debris-flow event (10 September 2019 - 10 September 2020) whose epicentres

375 are less than 200 km away from the Zelunglung. However, not all earthquakes influenced the instability of Zhelunglung's

376 glaciers and hillslopes. Keefer (1984) presented an upper bound curve of maximum distance from epicenter to disrupted slide

377 or fall (**Fig. 15**). Since 1940, only 12 earthquakes within a 420-km radius of ZLL fall below the bound curve, including the

378 1947 earthquake, the 1950 Assam earthquake and its aftershocks, the 1985 earthquake, and the 2017 Milin earthquake. If

379 including the inundated area of ~0.78 km^2 in 1950, the alluvial area disturbed by debris flows or floods decreased until 1990

380 and then kept at a low value before 2020 (**Fig. 14d**). If the 1950 debris-flow event was directly triggered by the 1950 Assam

381 earthquake, as Zhang (1992) suggested, the earthquake effect becomes negligible 40 years later. None of the other earthquakes

382 significantly influenced the 1968 and 1984 debris-flow events, even if 13 earthquakes of $Mw > 5.1$ occurred in 1968 and 6

383 earthquakes of $Mw \geq 4.5$ occurred in 1984. The 2017 Mw 6.4 Milin earthquake, of which the epicenter is 24 km from the

384 Zelunglung, probably has limited influence on its glacial activity because there is no report or sign on such glacier-related

385 hazards in the Zelunglung. However, there are direct proofs that the Milin earthquake caused the 2018 glacier surges and extra

386 large-scale debris flows in the Sedongpu (Hu et al., 2019; Zhang et al., 2022b), 25 km downstream of the Zelunglung.

387 Furthermore, we extracted the gridded mean values of annual mean air temperature, summer air temperature, annual

388 precipitation, and summer precipitation within the Zelunglung catchment during 1940 - 2021 from a 1-km monthly mean

389 temperature dataset for China (1901-2021) (Peng, 2019) and 1-km monthly precipitation dataset for China (1901-2021) (Peng,

390 2020), respectively (**Fig. 14b and c**). These data were validated using 496 independent meteorological observation points

391 (Peng et al., 2019). From 1940 to 2017, the annual mean and summer air temperatures at the Zelunglung kept relatively stable.

392 However, in 2018, there was a sudden and significant increase in the annual mean and summer air temperatures, with an

393   amplitude exceeding 2.5 ℃. Since then, the temperatures have maintained at a high level. There has been no significant change

394   in annual and summer precipitation since 1940, but a slight decreasing trend has been observed since 2000. The rates of

395   atmospheric warming in the Tibetan and Himalayan regions are far higher than the general global warming rate since 1960,

396   which accelerates the rates of most glaciers shrinking and ice mass loss across the regions (Shugar et al., 2021; Zhang et al.,

397   2020). Undoubtedly, the on-going warming increases the frequency of such glacier-related slope failures. The number of

398   rockfalls per decade show a similar growing trend with mean annual air temperature in Chamonix, Mont Blanc massif, France

399   since 1934 (Deline et al., 2015). Shugar et al. (2021) suggested that the 2021 Chamoli catastrophic mass flow resulted from a

400   complex response of the geologic and topographic settings to regional climate change. Even though there is no direct

401   observation data of surface temperature in the Zelunglung highland, the three years of warming may change the thermal and

402   hydrological conditions of the Zelunglung's glaciers, such as the thermal regime at the rock-ice contact surface, melting rate

403   of the surface ice and snow, englacial drainage system, fostering the instability of ice-rock blocks on the top. Previous intense

404   seimic shaking could widen rock fractures and reduce the ice-rock strength. It is no doubt that the 2020 Zelunglung event is

405   the product of the interplay among geological movement, steep topography, and climate warming. However, based on the fact

406   that the trend of the 1990-2020 NVAs shows a good agreement with that of the air temperature in the same period, it is likely

407   that the 2020 event was driven by the recent local warming rather than by geological events such as the mass flow event in
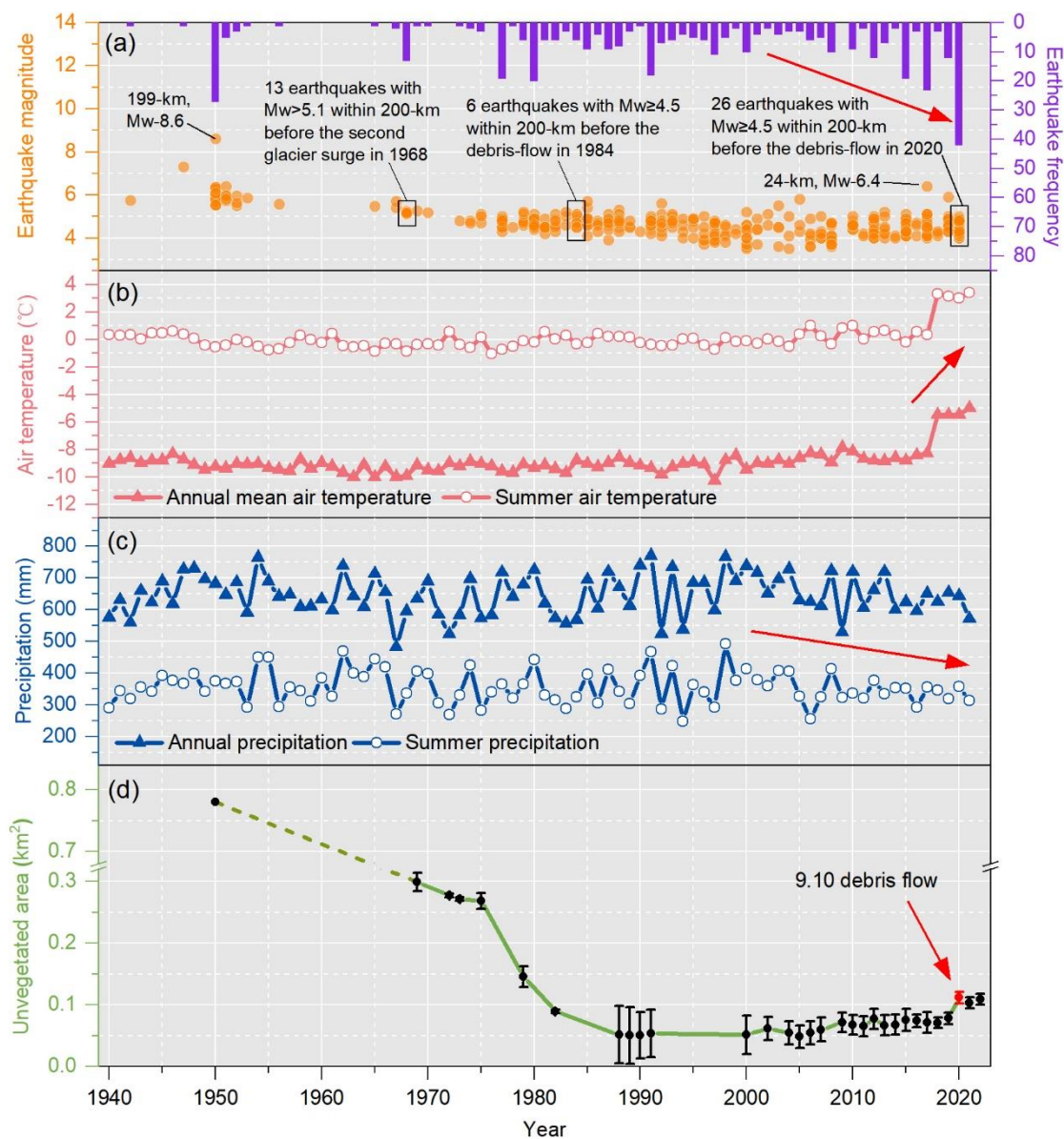
408   1950.

Figure 14: (a) Seismic events within a 200 km distance to the Zelunglung from 1940 to the present. (b) Changes in the annual mean and summer air temperatures in the Zelunglung from 1940 to the present. (c) Changes in the annual and summer precipitation in the Zelunglung from 1940 to the present. (d) Changes in the non-vegetated area of the Zelunglung alluvial fan from 1969 to the present (although the deposition of the 1950 event did not happen at the Zelunglung's outlet like the later events, we plot the NVA of the 1950 event as the starting point).
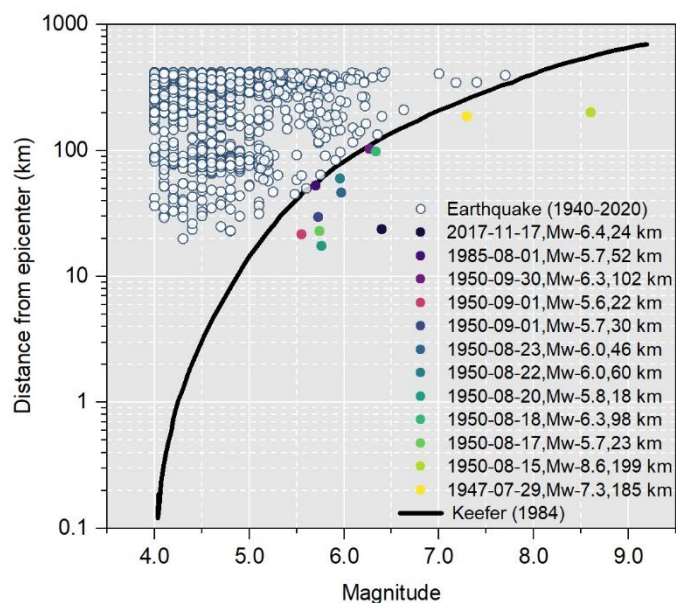
Figure 15: Distance from epicenters of the collected seismic events to the Zelunglung vs. the seismic magnitude (the black solid curve refers to Keefer (1984)).

6 Discussions

6.1 The dominant factor and future risk

It is evident that either earthquakes or climate change increase the occurrence of periglacial debris flows and their sediment yield. In the case of Zelunglung, the NVA closely related to the debris flows decreased until 1990 and slightly fluctuated around a low level until 2020. That means the effects of the 1950 earthquake were decaying; meanwhile, the local air temperature and precipitation had no significant variation until 2018. The response of hillslopes or glaciers to earthquakes is immediate. Had the 2017 Milin earthquake strongly impacted the glaciers in the Zelunglung, ice-rock failures would have happened a few months later, like in the Sedongpu catchment. By contrast, the response of glaciers to warming will take longer. We believe the abrupt 2.5 ℃ warming in 2018-2020 is dominant in initiating the 2020 ice-rock avalanche.

On the other hand, the magnitude of the warming-driven debris flows is smaller than that of the earthquake-driven. Zhang et al. (2022a) predicted that cryosphere degradation driving the increasing sediment yield in cold regions is likely to shift from a temperature-dependent regime toward a rainfall-dependent one in the next century. But in tectonically active high-altitude areas, the temperature-dependent and the earthquake-dependent regimes will alternate in the future.

The period of the Zelunglung glacier surges is getting shorter. Zhang (1985) supposed that the surging cycle of the Zelunglung glacier was about 20 years. According to the latest research by Guillet et al. (2022), the Zelunglung glacier showed signs of surge in 2004, 2005, and 2006. Moreover, there are more obvious signs of a surge in 2016 (**Fig. 16**). The interval between the last two surges is ten years, which shows that the surging cycle of the Zelunglung glacier may be decreasing, and the next

24

435 large-scale surge may happen in the next ten years. Furthermore, changes in the speed of glacier movement can strongly impact

436 channel side moraines or terminal moraines and lead to slope failures (Richardson and Reynolds, 2000). The potential ice

437 collapse area in the formation area of the Zelunglung catchment is 2.4 km², the rock collapse area reaches 0.96 km², and the

438 loose moraine accumulation reaches 5.2 km² (Liu et al., 2022; Li et al., 2021). However, the "9.10" debris flow was caused by

439 a relatively small area of ice-rock collapses in the formation area, which is only the tip of the iceberg compared to the overall

440 high-risk provenances in the formation area of the Zelunglung catchment. That means if intense earthquakes or extreme

441 warming events happen not far away from the catchment, the risk of slope failures or glacier detachment on the steep slopes

442 and ridges is high and huge amounts of sediment will bey transported into the river by large-scale debris flows.
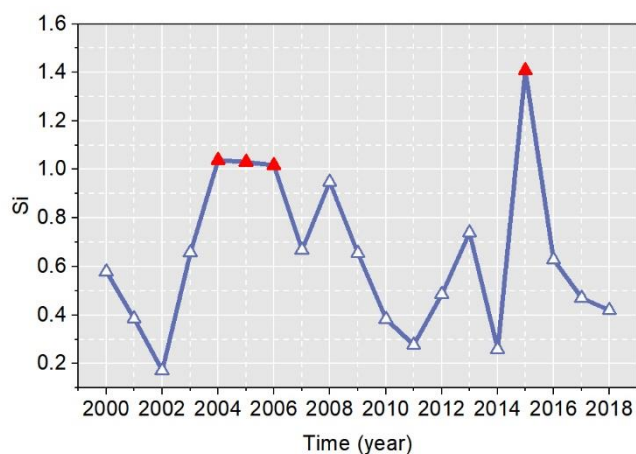
443

444 **Figure 16: Surge-index (S_i) of Zelunglung Glacier from 2000 to 2018. S_i is a quantitative index of the surge magnitude, calculated by**

445 **the formula** $s_i = \dfrac{IPR_i}{k \cdot V_0}$ **, where IPR_i is the inter-percentile range for year i, k is a threshold for surge identification, and V_0 is the error-**

446 **weighted mean velocity for the study year. The years with $S_i>1$ are marked with red triangles. (Data source:**

447 **https://doi.org/10.5281/zenodo.5524861 (Guillet et al., 2022)).**

448 **6.2 Effects on river geomorphology**

449 The moraine and old deposits on both channel sides provided numerous boulders for debris flows. The number of coarse

450 particles transported by the Zelunglung periglacial debris flows is very high, and there is no obvious particle sorting along the

451 flow path. Most of the boulders are gneiss with high hardness, and the wearing and disintegration effects are not significant

452 during the movement along the channel. Coarse particles are deposited on the platform at the bend and the top of the alluvial

453 fan, where the channel suddenly widens. Such phenomenon demonstrates that the movement, deposition, and particle size

454 distribution of the debris flow are not only related to the type of debris flow (Bardou et al., 2003) but also to topographic

455 conditions (Zhou et al., 2019; Ghilardi et al., 2001).

456 The deposition of the "9.10" debris flow narrowed the Yarlung Tsangpo River at the mouth of the Zelunglung, and the river

457 bed was significantly elevated. The river flow hardly transports the boulders on the alluvial fan. The peak discharge of the

458 largest flood in the Yarlung Tsangpo recorded by the hydrologic station at Nuxia, 40 km upstream of the Zelunglung, is 16800

459 m³/s. The maximum size of the particles in such a flood is about 150 cm. The floods capable of moving the coarsest boulders

460 (> 600 cm) deposited on the Zelunglung fan should be on the order of 10^6 m³/s of peak discharge (Lang et al., 2013). Such

461 high-magnitude floods in the Yarlung Tsangpo were caused by catastrophic breaching of landslide or glacial dams, e.g., several

462 Quaternary megafloods in the middle and downstream of Yarlung Tsangpo (Hu et al., 2018; Yang et al., 2022; Liu et al., 2015),

463 rather than caused by monsoonal runoffs. Modern outburst floods higher than 10^5 m³/s only happened on the Yigong River, a

464 downstream tributary of the Yarlung Tsangpo Gorge (Hu et al., 2021). Therefore, the time to evacuate the coarse sediments

465 on the alluvial fan is two orders of magnitude of the recurrence period of periglacial debris flows. The long-lived protruding

466 fan forms a knickpoint at the confluence. The repeated glacial and landslide dams in the margin of the Tibetan Plateau play

467 significant roles in reducing the river incision into the plateau interior together with the moraine dams in the glaciation ages

468 (Hu et al., 2021).

7 Conclusions

470 High-magnitude sediment evacuation by periglacial debris flows is a crucial surface process that links sediment yield from

471 high-altitude slopes to river sediment transportation. The ongoing glacier degradation in the Himalayan mountains in response

472 to recent earthquakes and climate increases the frequency of the debris flows and their sediment volume. The Zelunglung

473 catchment in the tectonically active eastern Himalayan syntaxis with a high uplift rate has recorded five periglacial debris flow

474 events since 1950. These events delivered huge volumes of sediment into the Yarlung Tsangpo River. We examine the history

475 of the five events and their sediment characteristics, especially the ice-rock-avalanche-triggered event in 2020, through field

476 investigations and remote sensing interpretations. Some findings are concluded as follows:

477 a) The periglacial debris flows have great capacities to erode channels, transport sediment, and impact obstacles. The

478 maximum values of the erosion depth, the erosion width, and the impact force near the Zelunglung's outlet are about 20

479 m, 14 m, and $3.64×10^6$ kN, respectively, in the 2020 event. The debris flows transported a high concentration of coarse

480 grains with the size > 50 cm. The 100-300 cm grains account for 77.4% of the coarse grains.

481 b) Most of the angular rocks moved by the 2020 avalanche were not delivered downward further. The boulders transported

482 by subsequent debris flows probably originated from the middle of the downstream reaches. The grain size segregation

483 was not observed between the middle reach and the alluvial channel.

484 c) The non-vegetated area of the Zelunglung's fan reduced from 0.78 km² in 1950 to 0.067 km² in 1990, indicating the

485 influence of the 1950 earthquake on the debris-flow sediment transportation could last 40 years and keep at a stable low

486 value until 2020.

487 d) The seismic and local meteorological data show that the recent warming events drove the 2020 debris-flow event during

488 2018-2020. The surging cycle of Zelunglung's glaciers is getting short due to climate change. The correspondence between

489 the recent increases in the local air temperature and the NVA implies that the debris flow occurrences transfer from the

490 tectonic-driven to the climatic-driven.

491

492

496

Data availability. All raw data can be provided by the corresponding authors upon request.

498

Author contributions. KHH conceptualized the study, interpreted the images, wrote and edited the manuscript. HL analyzed the data and wrote the manuscript draft. KHH, HL, SL, LW, XPZ, and BZ performed the field surveys. HL and MRG collected satellite and background data. LMZ provided constructive suggestions. All authors contributed to the preparation and editing of the paper.

503

Competing interests. The authors declare that they have no conflict of interest

References

Anacona, P. I., Mackintosh, A., and Norton, K. P.: Hazardous processes and events from glacier and permafrost areas: lessons from the Chilean and Argentinean Andes, Earth Surf Proc Land, 40, 2-21, 10.1002/esp.3524, 2015.

Bajracharya, S. R. and Mool, P.: Glaciers, glacial lakes and glacial lake outburst floods in the Mount Everest region, Nepal, Ann Glaciol, 50, 81-86, Doi 10.3189/172756410790595895, 2009.

Bardou, E., Ancey, C., Bonnard, C., and Vulliet, L.: Classification of debris-flow deposits for hazard assessment in alpine areas, 3rd International Conference on Debris-Flow Hazards Mitigation, Davos, SWITZERLAND, 2003
Sep 10-12, WOS:000189451200068, 799-808, 2003.

Chen, D., Xu, B., Yao, T., Guo, Z., Cui, P., Chen, F., Zhang, R., ZHANG, X., ZHANG, Y., and FAN, J.: Assessment of past, present and future environmental changes on the Tibetan Plateau, Chinese Science Bulletin, 60, 3025-3035, 2015.

Chen, N., Yang, C., Li, Z., and He, j.: Research On the Relationship between the Calculation of Debris flow Velocity and Its Super Elevation in Bend, Journal of Sichuan University. Engineering Science Edition, 41, 165-171, 2009.

Costa, J. E.: Paleohydraulic reconstruction of flash-flood peaks from boulder deposits in the colorado front range, Geol. Soc. Am. Bull., 94, 986-1004, 10.1130/0016-7606(1983)94<986:Profpf>2.0.Co;2, 1983.

Cui, P., Zhou, G. G. D., Zhu, X. H., and Zhang, J. Q.: Scale amplification of natural debris flows caused by cascading landslide dam failures, Geomorphology, 182, 173-189, 10.1016/j.geomorph.2012.11.009, 2013.

Cui, Y. L., Hu, J. H., Xu, C., Miao, H. B., and Zheng, J.: Landslides triggered by the 1970 Ms 7.7 Tonghai earthquake in Yunnan, China: an inventory, distribution characteristics, and tectonic significance, J Mt. Sci., 19, 1633-1649, 10.1007/s11629-022-7321-x, 2022.

David, R., Montgomery, and, Bernard, Hallet, and, Liu, Yuping, and and: Evidence for Holocene megafloods down the Tsangpo River gorge, southeastern Tibet, Quaternary Res, 2004.

Deline, P., Gruber, S., Delaloye, R., Fischer, L., Geertsema, M., Giardino, M., Hasler, A., Kirkbride, M., Krautblatter, M., Magnin, F., McColl, S., Ravanel, L., and Schoeneich, P.: Chapter 15 - Ice Loss and Slope Stability in High-Mountain Regions, in: Snow and Ice-Related Hazards, Risks, and Disasters, edited by: Shroder, J. F., Haeberli, W., and Whiteman, C., Academic Press, Boston, 521-561, https://doi.org/10.1016/B978-0-12-394849-6.00015-9, 2015.

530   Ding, L., Zhong, D. L., Yin, A., Kapp, P., and Harrison, T. M.: Cenozoic structural and metamorphic evolution of the eastern
531   Himalayan syntaxis (Namche Barwa), Earth Planet Sc Lett, 192, 423-438, Doi 10.1016/S0012-821x(01)00463-0, 2001.
532   Evans, S. G. and Clague, J. J.: Recent climatic-change and catastrophic geomorphic processes in mountain environments,
533   Geomorphology, 10, 107-128, 10.1016/0169-555x(94)90011-6, 1994.
534   Ghilardi, P., Natale, L., and Savi, F.: Modeling debris flow propagation and deposition, Phys Chem Earth Pt C, 26, 651-656,
535   Doi 10.1016/S1464-1917(01)00063-0, 2001.
536   Guillet, G., King, O., Lv, M. Y., Ghuffar, S., Benn, D., Quincey, D., and Bolch, T.: A regionally resolved inventory of High
537   Mountain Asia surge-type glaciers, derived from a multi-factor remote sensing approach, Cryosphere, 16, 603-623, 10.5194/tc-
538   16-603-2022, 2022.
539   Haeberli, W., Whiteman, C. A., and Shroder, J. F.: Snow and ice-related hazards, risks, and disasters, Academic Press Waltham,
540   MA2014.
541   Han, L. M. and Feng, Q. N.: Developmental characteristics and genetic mechanism of debris flow in Zelunglung Glacier,
542   Nanga Bawa Peak, Inner Mongolia Science Technology & Economy, 58-59, 2018.
543   Hu, G., Yi, C. L., Liu, J. H., Wang, P., Zhang, J. F., Li, S. H., Li, D. H., Huang, J. W., Wang, H. Y., Zhang, A. M., Shi, L. F.,
544   and Shui, X. J.: Glacial advances and stability of the moraine dam on Mount Namcha Barwa since the Last Glacial Maximum,
545   eastern Himalayan syntaxis, Geomorphology, 365, 14, 10.1016/j.geomorph.2020.107246, 2020.
546   Hu, H. P., Feng, J. L., and Chen, F.: Sedimentary records of a palaeo-lake in the middle Yarlung Tsangpo: Implications for
547   terrace genesis and outburst flooding, Quat. Sci. Rev., 192, 135-148, 10.1016/j.quascirev.2018.05.037, 2018.
548   Hu, K., Wu, C., Wei, L., Zhang, X., Zhang, Q., Liu, W., and Yanites, B. J.: Geomorphic effects of recurrent outburst
549   superfloods in the Yigong River on the southeastern margin of Tibet, Sci Rep, 11, 10.1038/s41598-021-95194-1, 2021.
550   Hu, K. H., Zhang, X. P., You, Y., Hu, X. D., Liu, W. M., and Li, Y.: Landslides and dammed lakes triggered by the 2017
551   Ms6.9 Milin earthquake in the Tsangpo gorge, Landslides, 16, 993-1001, 10.1007/s10346-019-01168-w, 2019.
552   Huang, S. Y., Chen, Y. G., Burr, G. S., Jaiswal, M. K., Lin, Y. N., Yin, G. M., Liu, J. W., Zhao, S. J., and Cao, Z. Q.: Late
553   Pleistocene sedimentary history of multiple glacially dammed lake episodes along the Yarlung-Tsangpo river, southeast Tibet,
554   Quaternary Res, 82, 430-440, 10.1016/j.yqres.2014.06.001, 2014.
555   Huggel, C.: Assessment of glacial hazards based on remote sensing and GIS modeling, University of Zurich, Zürich2004.
556   Huggel, C., Haeberli, W., Kaab, A., Bieri, D., and Richardson, S.: An assessment procedure for glacial hazards in the Swiss
557   Alps, Can Geotech J, 41, 1068-1083, 10.1139/t04-053, 2004.
558   Jia, H., Chen, F., and Pan, D.: Disaster chain analysis of avalanche and landslide and the river blocking dam of the Yarlung
559   Zangbo River in Milin County of Tibet on 17 and 29 October 2018, Int. J. Environ. Res. Public Health, 16, 4707,
560   10.3390/ijerph16234707, 2019.
561   Kääb, A. and Girod, L.: Brief communication: Rapid ∼ 335 x 10^6 m^3 bed erosionafter
562   detachment of the Sedongpu Glacier (Tibet), Cryosphere, 17, 2533-2541, 10.5194/tc-17-2533-2023, 2023.
563   Kääb, A., Jacquemart, M., Gilbert, A., Leinss, S., Girod, L., Huggel, C., Falaschi, D., Ugalde, F., Petrakov, D., and
564   Chernomorets, S.: Sudden large-volume detachments of low-angle mountain glaciers–more frequent than thought?, The
565   Cryosphere, 15, 1751-1785, 2021.
566   Kargel, J. S., Leonard, G. J., Shugar, D. H., Haritashya, U. K., Bevington, A., Fielding, E. J., Fujita, K., Geertsema, M., Miles,
567   E. S., Steiner, J., Anderson, E., Bajracharya, S., Bawden, G. W., Breashears, D. F., Byers, A., Collins, B., Dhital, M. R.,
568   Donnellan, A., Evans, T. L., Geai, M. L., Glasscoe, M. T., Green, D., Gurung, D. R., Heijenk, R., Hilborn, A., Hudnut, K.,
569   Huyck, C., Immerzeel, W. W., Liming, J., Jibson, R., Kaab, A., Khanal, N. R., Kirschbaum, D., Kraaijenbrink, P. D., Lamsal,
570   D., Shiyin, L., Mingyang, L., McKinney, D., Nahirnick, N. K., Zhuotong, N., Ojha, S., Olsenholler, J., Painter, T. H., Pleasants,
571   M., Pratima, K. C., Yuan, Q. I., Raup, B. H., Regmi, D., Rounce, D. R., Sakai, A., Donghui, S., Shea, J. M., Shrestha, A. B.,
572   Shukla, A., Stumm, D., van der Kooij, M., Voss, K., Xin, W., Weihs, B., Wolfe, D., Lizong, W., Xiaojun, Y., Yoder, M. R.,
573   and Young, N.: Geomorphic and geologic controls of geohazards induced by Nepal's 2015 Gorkha earthquake, Science, 351,
574   aac8353, 10.1126/science.aac8353, 2016.
575   Keefer, D. K.: Landslides caused by earthquakes, Geol. Soc. Am. Bull., 95, 406-421, 10.1130/0016-
576   7606(1984)95<406:Lcbe>2.0.Co;2, 1984.
577   Krautblatter, M., Funk, D., and Günzel, F. K.: Why permafrost rocks become unstable: a rock–ice-mechanical model in time
578   and space, Earth Surf Proc Land, 38, 876-887, 10.1002/esp.3374, 2013.

579 Lang, K. A., Huntington, K. W., and Montgomery, D. R.: Erosion of the Tsangpo Gorge by megafloods, Eastern Himalaya,
580 Geology, 41, 1003-1006, 10.1130/g34693.1, 2013.
581 Larsen, I. J., Montgomery, D. R., and Korup, O.: Landslide erosion controlled by hillslope material, Nat. Geosci., 3, 247-251,
582 10.1038/ngeo776, 2010.
583 Li, H., HU, K. H., Zhang, X. P., Liu, S., and Wei, L.: Causes and Damage of the 2020 Periglacial Debris Flows at Zelunglung
584 Catchment in the Eastern Syntaxis of Himalaya, The XIV Congress of the International Association for Engineering Geology
585 and the Environment, Chengdu, China, 2023(Preprint).
586 Li, J., Chu, H., Li, B., Gao, Y., Wang, M., Zhao, C., and Liu, X.: Analysis of development characteristics of high-
587 elevationchain geological hazard in Zelongnong, Nyingchi, Tibet based on high resolution image and InSAR interpretation,
588 The Chinese Journal of Geological Hazard and Control, 32, 9, 2021.
589 Li, W. L., Zhao, B., Xu, Q., Scaringi, G., Lu, H. Y., and Huang, R. Q.: More frequent glacier-rock avalanches in Sedongpu
590 gully are blocking the Yarlung Zangbo River in eastern Tibet, Landslides, 19, 1-13, 10.1007/s10346-021-01798-z, 2022.
591 Li, Y., Yan, C., Hu, K., and Wei, L.: Variation of hazard areas of typical rainstorm debris flow alluvial fans, Resources and
592 Environment in the Yangtze Basin, 26, 789-796, 2017.
593 Liu, M., Zhang, Y., Tian, S. F., Chen, N. S., Mahfuzr, R., and Javed, I.: Effects of loose deposits on debris flow processes in
594 the Aizi Valley, southwest China, J Mt. Sci., 17, 156-172, 10.1007/s11629-019-5388-9, 2020.
595 Liu, W., Wang, M., Song, B., Yu, T., Huang, X., Jiang, Y., and Sun, Y.: Surveys and chain structure study of potential hazards
596 of ice avalanches based on optical remote sensing technology: A case study of southeast Tibet, Remote Sensing for Natural
597 Resources, 34, 265-276, 2022.
598 Liu, W. M., Lai, Z. P., Hu, K. H., Ge, Y. G., Cui, P., Zhang, X. G., and Liu, F.: Age and extent of a giant glacial-dammed lake
599 at Yarlung Tsangpo gorge in the Tibetan Plateau, Geomorphology, 246, 370-376, 10.1016/j.geomorph.2015.06.034, 2015.
600 Liu, Y., Montgomery, D. R., Hallet, B., Tang, W., Zhang, J., and Zhang, X.: Quaternary Glacier Blocking Events at the
601 Entrance of Yarlung Zangbo Great Canyon, Southeast Tibet, Quaternary Sciences, 26, 52-62. (in Chinese), 2006.
602 Major, J. J.: Pebble orientation on large, experimental debris-flow deposits, Sediment Geol, 117, 151-164, Doi 10.1016/S0037-
603 0738(98)00014-1, 1998.
604 McCoy, S. W., Tucker, G. E., Kean, J. W., and Coe, J. A.: Field measurement of basal forces generated by erosive debris flows,
605 J. Geophys. Res.-Earth Surf., 118, 589-602, 10.1002/jgrf.20041, 2013.
606 Peng, D. L., Zhang, L. M., Jiang, R. C., Zhang, S., Shen, P., Lu, W. J., and He, X.: Initiation mechanisms and dynamics of a
607 debris flow originated from debris-ice mixture slope failure in southeast Tibet, China, Eng. Geol., 307, 17,
608 10.1016/j.enggeo.2022.106783, 2022.
609 Peng, S. Z.: 1-km monthly mean temperature dataset for china (1901-2021), A Big Earth Data Platform for Three Poles
610 [dataset], 10.11888/Meteoro.tpdc.270961, 2019.
611 Peng, S. Z.: 1-km monthly precipitation dataset for China (1901-2021), A Big Earth Data Platform for Three Poles [dataset],
612 10.5281/zenodo.3185722, 2020.
613 Peng, S. Z., Ding, Y. X., Liu, W. Z., and Li, Z.: 1 km monthly temperature and precipitation dataset for China from 1901 to
614 2017, Earth Syst Sci Data, 11, 1931–1946, 10.5194/essd-11-1931-2019, 2019.
615 Petrakov, D. A., Krylenko, I. V., Chernomorets, S. S., Tutubalina, O. V., Krylenko, I. N., and Shakhmina, M. S.: Debris flow
616 hazard of glacial lakes in the Central Caucasus, 4th International Conference on Debris-Flow Hazards Mitigation - Mechanics,
617 Prediction and Assessment, Chengdu, PEOPLES R CHINA, 2007
618 Sep 10-13, WOS:000267333300068, 703-+, 2007.
619 Richardson, S. D. and Reynolds, J. M.: An overview of glacial hazards in the Himalayas, Quatern Int, 65, 31-47, Doi
620 10.1016/S1040-6182(99)00035-X, 2000.
621 Shen, Y., Su, H., Wang, G., Mao, W., Wang, S., Han, P., Wang, N., and Li, Z.: The Responses of Glaciers and Snow Cover to
622 Climate Change in Xinjiang (II): Hazards Effects, Journal of Glaciology and Geocryology, 35, 1355-1370,
623 10.1161/01.cir.45.6.1150, 2013.
624 Shugar, D. H., Jacquemart, M., Shean, D., Bhushan, S., Upadhyay, K., Sattar, A., Schwanghart, W., McBride, S., de Vries, M.
625 V. W., Mergili, M., Emmer, A., Deschamps-Berger, C., McDonnell, M., Bhambri, R., Allen, S., Berthier, E., Carrivick, J. L.,
626 Clague, J. J., Dokukin, M., Dunning, S. A., Frey, H., Gascoin, S., Haritashya, U. K., Huggel, C., Kaab, A., Kargel, J. S.,
627 Kavanaugh, J. L., Lacroix, P., Petley, D., Rupper, S., Azam, M. F., Cook, S. J., Dimri, A. P., Eriksson, M., Farinotti, D., Fiddes,
628 J., Gnyawali, K. R., Harrison, S., Jha, M., Koppes, M., Kumar, A., Leinss, S., Majeed, U., Mal, S., Muhuri, A., Noetzli, J.,

629 Paul, F., Rashid, I., Sain, K., Steiner, J., Ugalde, F., Watson, C. S., and Westoby, M. J.: A massive rock and ice avalanche
630 caused the 2021 disaster at Chamoli, Indian Himalaya, Science, 373, 300-+, 10.1126/science.abh4455, 2021.
631 Sohn, Y. K.: Coarse-grained debris-flow deposits in the Miocene fan deltas, SE Korea: a scaling analysis, Sediment Geol, 130,
632 45-64, Doi 10.1016/S0037-0738(99)00099-8, 2000.
633 Tian, L. D., Yao, T. D., Gao, Y., Thompson, L., Mosley-Thompson, E., Muhammad, S., Zong, J. B., Wang, C., Jin, S. Q., and
634 Li, Z. G.: Two glaciers collapse in western Tibet, J Glaciol, 63, 194-197, 10.1017/jog.2016.122, 2017.
635 Wang, P., Wang, H., Hu, G., Qin, J., and Li, C.: A preliminary study on the development of dammed paleolakes in the Yarlung
636 Tsangpo River basin, southeastern Tibet, Earth Science Frontiers, 28, 035-045, 2021.
637 Wang, Z., Hu, K. H., and Liu, S.: Classification and sediment estimation for debris flow-prone catchments in the Parlung
638 Zangbo Basin on the southeastern Tibet, Geomorphology, 413, 14, 10.1016/j.geomorph.2022.108348, 2022.
639 Ward, F. K.: Explorations in south-eastern Tibet, The Geographical Journal, 67, 97-119, 1926.
640 Yan, Y., Tang, H., Hu, K. H., Turowski, J. M., and Wei, F. Q.: Deriving Debris-Flow Dynamics From Real-Time Impact-
641 Force Measurements, J. Geophys. Res.-Earth Surf., 128, 24, 10.1029/2022jf006715, 2023.
642 Yang, A. N., Wang, H., Liu, W. M., Hu, K. H., Liu, D. Z., Wu, C. H., and Hu, X. D.: Two megafloods in the middle reach of
643 Yarlung Tsangpo River since Last-glacial period: Evidence from giant bars, Glob. Planet. Change, 208, 18,
644 10.1016/j.gloplacha.2021.103726, 2022.
645 Yu, G. A., Yao, W., Huang, H. Q., and Liu, Z.: Debris flows originating in the mountain cryosphere under a changing climate:
646 A review, Prog. Phys. Geogr., 45, 339-374, 2021.
647 Zhang, G. Q., Yao, T. D., Xie, H. J., Yang, K., Zhu, L. P., Shum, C. K., Bolch, T., Yi, S., Allen, S., Jiang, L. G., Chen, W. F.,
648 and Ke, C. Q.: Response of Tibetan Plateau lakes to climate change: Trends, patterns, and mechanisms, Earth-Sci. Rev., 208,
649 22, 10.1016/j.earscirev.2020.103269, 2020.
650 Zhang, J. S. and Shen, X. J.: Debris-flow of Zelongnong Ravine in Tibet, J Mt. Sci., 8, 535-543, 10.1007/s11629-011-2137-0,
651 2011.
652 Zhang, T., Li, D. F., East, A. E., Walling, D. E., Lane, S., Overeem, I., Beylich, A. A., Koppes, M., and Lu, X. X.: Warming-
653 driven erosion and sediment transport in cold regions, Nat Rev Earth Env, 3, 832-851, 10.1038/s43017-022-00362-0, 2022a.
654 Zhang, W. J.: Some features of the surge glacier in the MT. Namjagbarwa, Mountain Research, 46-50, 1985.
655 Zhang, W. J.: Identification of glaciers with surge characteristics on the Tibetan Plateau, Ann Glaciol, 16, 168-172, 1992.
656 Zhang, X. P., Hu, K. H., Liu, S., Nie, Y., and Han, Y. Z.: Comprehensive interpretation of the Sedongpu glacier-related mass
657 flows in the eastern Himalayan syntaxis, J Mt. Sci., 19, 2469-2486, 10.1007/s11629-022-7376-8, 2022b.
658 Zhou, G. G. D., Li, S., Song, D. R., Choi, C. E., and Chen, X. Q.: Depositional mechanisms and morphology of debris flow:
659 physical modelling, Landslides, 16, 315-332, 10.1007/s10346-018-1095-9, 2019.
660 Zhu, S., Wu, Z. H., Zhao, X. T., Li, J. P., and Wang, H.: Middle-Late Pleistocene Glacial Lakes in the Grand Canyon of the
661 Tsangpo River, Tibet, Acta Geol Sin-Engl, 86, 266-283, 10.1111/j.1755-6724.2012.00627.x, 2012.

662